Advance Publication by J-STAGE

Journal of Thermal Science and Technology

DOI: 10.1299/jtst.25-00210

Received date : 1 July, 2025

Accepted date : 2 October, 2025

J-STAGE Advance Publication date : 12 October, 2025

Spanwise confinement effects on a stably stratified shear layer

Takumi AKAO*, Tomoaki WATANABE* and Koji Nagata*
*Department of Mechanical Engineering and Science, Kyoto University
Kyotodaigaku-Katsura, Nishikyo-ku, Kyoto-shi, Kyoto 615-8530, Japan
E-mail:akao.takumi.33a@st.kyoto-u.ac.jp

Abstract
Direct numerical simulations (DNS) are conducted to investigate the effects of spanwise domain size on stably stratified turbulent shear layers. The focus is on the formation and spatial organization of elongated large-scale structures (ELSS), which emerge following the transition from Kelvin–Helmholtz instability and characterized by streamwise extents far exceeding the shear layer's thickness. Simulations are conducted for a temporally developing shear layer under stable density stratification. The spanwise extent is varied, while the streamwise and vertical domain sizes are fixed. Flow visualizations, one-point statistics, energy spectra, and two-point correlation functions are used to assess the influence of spanwise confinement on the transition process and late-time turbulence characteristics. The results show that when the spanwise domain size is very small, the transition process is altered and ELSS fail to develop properly. For intermediate domain sizes, the streamwise elongation of ELSS is captured, but their meandering and spatial repetition are suppressed. Statistical analysis reveals that while the meandering of ELSS contributes to large-scale structure, the presence of multiple alternating ELSS in the spanwise direction is more critical to the overall flow statistics. These findings emphasize the importance of spanwise configurations of ELSS in the dynamics and energetics of stably stratified shear layers.

Keywords : Turbulent shear layer, Stably stratified turbulence, Direct numerical simulation

1. Introduction

Turbulence with thermal stratification is widely observed in environmental and engineering contexts. In particular, temperature variations induce buoyancy effects on turbulence. When the density field is stably stratified, buoyancy suppresses vertical turbulent motions. Nevertheless, even in stably stratified fluids, mean shear often generates turbulence via Kelvin–Helmholtz (KH) instability (Smyth and Moum, 2000, 2012). At large values of Prandtl numbers, defined as the ratio of kinematic viscosity to thermal diffusivity, Holmboe instabilities can also initiate turbulence (Smyth and Winters, 2003; Smyth et al., 2007; Salehipour et al., 2016). Turbulence plays a critical role in momentum and heat transport, influencing the development of the flow itself. Since turbulent shear layers in stably stratified fluids are commonly encountered in practical environmental and engineering applications, they have attracted significant attention in previous studies.

Direct numerical simulations (DNS) have been employed to investigate stably stratified turbulent shear layers, revealing various flow characteristics. Some studies have examined the KH instability process, which begins with the formation of spanwise vortices and evolves through secondary instabilities into fully three-dimensional turbulence (Mashayek and Peltier, 2012a, 2012b; Watanabe and Nagata, 2021; Fritts et al., 2022). Other studies have focused on the turbulent structures in the fully developed turbulent shear layer, confirming the presence of highly elongated large-scale structures (ELSS) (Watanabe et al., 2019a). These ELSS are characterized by streamwise lengths much larger than the vertical thickness of the shear layer and carry a significant portion—approximately 50%—of the total turbulent kinetic energy, thereby influencing the flow energetics (Watanabe and Nagata, 2021).

The ELSS manifest as alternating long patterns of positive and negative velocity fluctuations in the horizontal plane. These velocity patterns, appearing alternately in the spanwise direction, dominate the large-scale spanwise velocity fluctuations. The spanwise organization of ELSS is expected to be therefore crucial to the development of the flow. The

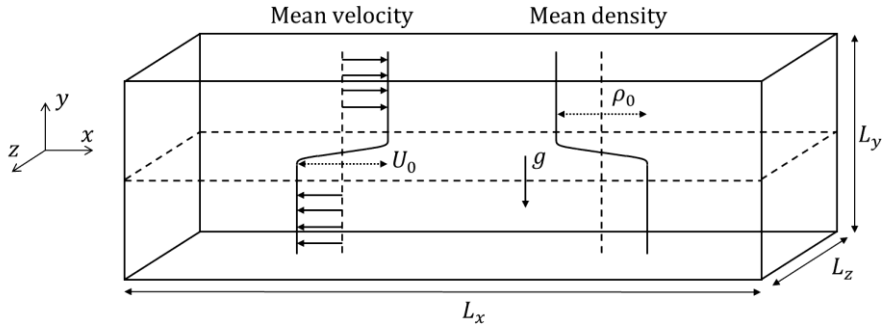

Fig. 1 A schematic of the computational domain and the stably stratified shear layer.

Table 1 Computational parameters.

Case	L_x/h_0	L_y/h_0	L_z/h_0	N_x	N_y	N_z	N_e
Lz07	448	80	7	7776	700	128	23
Lz14	448	80	14	7776	700	243	12
Lz28	448	80	28	7776	700	486	6
Lz42	448	80	42	7776	700	729	4
Lz56	448	80	56	7776	700	972	3
Lz84	448	80	84	7776	700	1458	2
Lz14f	448	80	14	9332	840	293	1

present study employs DNS to investigate the spanwise organization of ELSS and its influence on the statistical properties of stably stratified shear layers. Specifically, DNS is conducted with varying spanwise domain sizes. When the domain size is too small, the spanwise organization of the ELSS is significantly altered. Comparisons among different spanwise domain sizes reveal confinement effects in the spanwise direction, elucidating the role of ELSS organization in flow evolution. While such effects observed in small domains with periodic boundaries are often referred to as “confinement effects” in the turbulence literature (Gualtieri and Meneveau, 2010; Zhai and Yeung, 2018; McMullan et al., 2024), we note that, from the perspective of numerical simulations, they originate from artificial effects of finite domain sizes. The present approach, which involves artificially modifying flow fields, has been widely used in previous turbulence studies. For instance, the origin of large-scale vortices in turbulent wakes was examined by suppressing Kármán vortices using porous structures (Cimbala et al., 1988). The role of internal shear instability in small-scale turbulence was studied using DNS of turbulence with artificially imposed velocity perturbations to trigger small-scale shear instability (Watanabe, 2024; Watanabe and Nagata, 2025). Similarly, the role of large-scale motions in wall turbulence was investigated using simulations with small computational domains (Jiménez and Moin, 1991). In the present study, we demonstrate that the spanwise distribution of ELSS plays a critical role in the temporal evolution of velocity statistics.

2. Direct numerical simulations

Direct numerical simulations (DNS) are performed for a temporally developing shear layer under stable density stratification. The governing equations are the incompressible Navier–Stokes equations with the Boussinesq approximation, given as follows:

$$\frac{\partial u_j}{\partial x_j} = 0, \tag{1}$$

$$\frac{\partial u_i}{\partial t} + \frac{\partial u_i u_j}{\partial x_j} = -\frac{1}{\rho_a}\frac{\partial p}{\partial x_i} + \nu\frac{\partial^2 u_i}{\partial x_j \partial x_j} - g\frac{\rho}{\rho_a}\delta_{i2}, \tag{2}$$

$$\frac{\partial \rho}{\partial t} + \frac{\partial u_j \rho}{\partial x_j} = \kappa\frac{\partial^2 \rho}{\partial x_j \partial x_j}, \tag{3}$$

where the subscripts $i, j = 1, 2, 3$ correspond to the x, y, and z directions, respectively. Here, t denotes time, p is pressure, ν is the kinematic viscosity, κ is the diffusivity coefficient for density, ρ_a is the reference density, and g is the gravitational acceleration. The gravitational force acts in the negative y direction and is represented using the Kronecker delta δ_{ij}. In the present Boussinesq formulation, Eq. (3) describes the advection–diffusion of the density fluctuation. For thermally stratified flows under a linear equation of state, this equation is equivalent to the temperature transport equation derived from the internal-energy balance, with the density fluctuation related to the temperature fluctuation via the thermal expansion coefficient (Smyth and Moum, 2000; Onishi and Komori, 2006; Watanabe et al., 2016). For solutal (e.g., salt) stratification, Eq. (3) corresponds to the concentration transport equation (Okino et al., 2021).

The simulations are performed using an in-house DNS code based on a fractional step method and finite difference schemes. Fully conservative finite difference schemes are employed for spatial discretization, with fourth-order accuracy in the horizontal directions and second-order accuracy in the vertical direction. Time integration is carried out using a third-order Runge–Kutta method, while the pressure Poisson equation is solved using the biconjugate gradient stabilized method. The present DNS code has been extensively validated in our previous studies of canonical turbulent flows, including jets (Hayashi et al., 2021a, 2021b), mixing layers (Watanabe and Nagata, 2017b), boundary layers (Watanabe et al., 2018c; Zhang et al., 2023), and grid turbulence (Watanabe and Nagata, 2018b; Watanabe et al., 2022; Nakamura et al., 2023). In these studies, detailed comparisons with experimental measurements demonstrated that the simulations accurately reproduced the flow behaviour, including statistics of velocity and passive scalars (temperature or species concentration) as well as the characteristic turbulent structures. A grid-dependence assessment of the numerical schemes employed here was presented in Watanabe et al. (2018a), where examinations of the enstrophy spectrum confirmed that small-scale turbulent motions are well resolved when the grid spacing is smaller than 2η with η denoting the Kolmogorov scale.

Figure 1 illustrates an overview of the computational domain, along with the mean profiles of streamwise velocity and density. This flow setup has widely been considered in previous studies (Smyth and Moum, 2000; Rahmani et al., 2014; Watanabe et al., 2019a). The computational domain size is defined as $L_x \times L_y \times L_z$. The streamwise, vertical, and spanwise directions are denoted by x, y, and z, and the corresponding velocity components are u, v, and w, respectively. The flow is statistically homogeneous in the horizontal directions and develops with time. Therefore, statistical quantities are defined as averages taken over horizontal planes and expressed as functions of y and time. The average of a variable f is denoted by $\langle f \rangle$, and the fluctuating component is defined as $f' = f - \langle f \rangle$. The root-mean-square value is defined by $f_{rms} = \langle f'^2 \rangle^{1/2}$. The initial mean streamwise velocity is prescribed as $\langle u \rangle = 0.5U_0 \tanh(y/h_0)$, where U_0 is the mean velocity jump across the shear layer and h_0 is the initial shear layer thickness. The initial mean velocities in the vertical and spanwise directions are set to zero. The initial density profile is given by $\rho = -0.5\rho_0 \tanh(y/h_0)$, where ρ_0 is the density jump across the shear layer. The initial velocity field is constructed by superimposing perturbations onto the mean streamwise velocity, resulting in $(u, v, w) = (\langle u \rangle + u', v', w')$. These perturbations are generated using random numbers with prescribed spatial correlations, following the procedure described in a previous study (Watanabe et al., 2019b). The perturbation length scale is $0.34h_0$ and root-mean-square (rms) velocity is $0.025U_0$. The shear layer evolves over time and remains statistically homogeneous in the streamwise and spanwise directions due to periodic boundary conditions imposed in both directions. Free-slip boundary conditions are applied at the upper and lower boundaries.

The Reynolds number $Re = U_0 h_0/\nu$, Prandtl number $Pr = \nu/\kappa$, and Richardson number $Ri = g\rho_0 h_0/\rho_a U_0^2$ are set to $Re = 1200$, $Ri = 0.06$, and $Pr = 1$, respectively. The dependence of the stably stratified shear layers with ELSS on Re and Ri has been investigated in prior studies (Watanabe et al., 2019a; Watanabe and Nagata, 2021). These studies showed that the ELSS formation is observed even at higher Re, and occurs when $Ri \geq 0.06$. The statistical features of stably stratified shear layers with ELSS were found to be similar across different values of Re and Ri, indicating that the current results are applicable for other parameter sets. Note that this study focuses on turbulent shear layers arising from KH instability. As $Pr > 1$ often leads to transition via Holmboe instability, high Prandtl number regimes are not considered here.

DNS is conducted for different L_z values to investigate the effects of the finite domain size. The details of the DNS parameters are shown in Tab. 1. The domain sizes in the x and y directions are kept constant across all cases. Both L_x and L_y are sufficiently large so as not to influence the flow evolution. The flow transitions into a turbulent state over

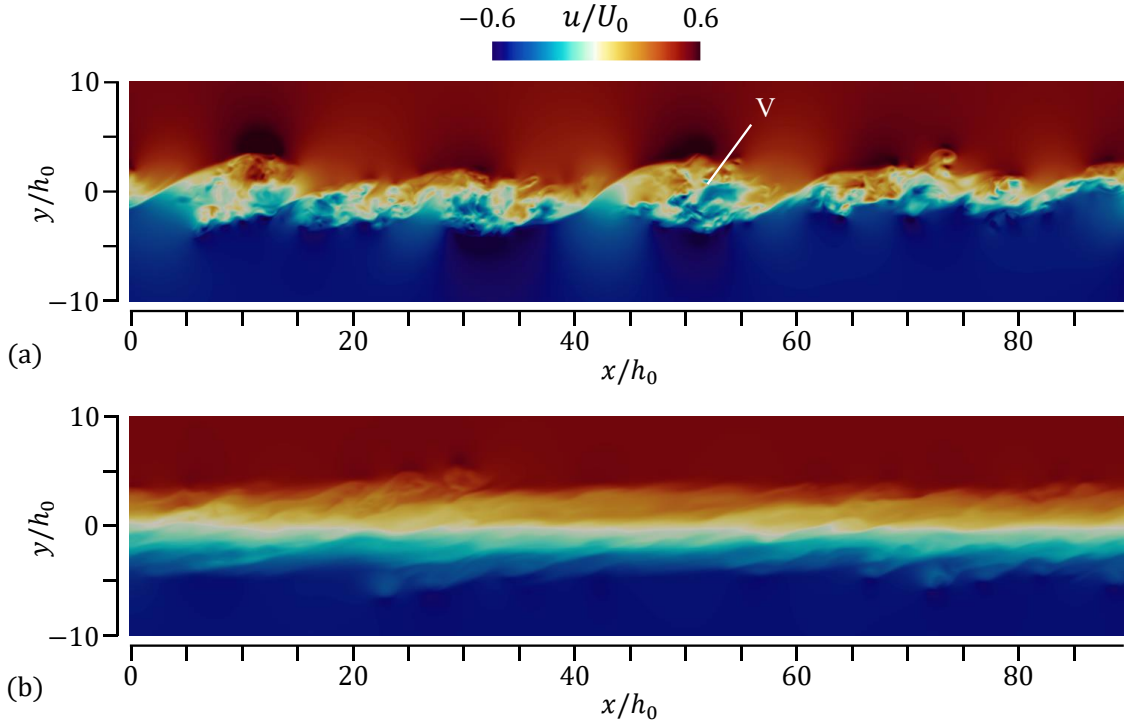

Fig. 2 Streamwise velocity profiles on an xy plane at (a) $t/t_r = 120$ and (b) $t/t_r = 320$ for $L_z = 7h_0$.

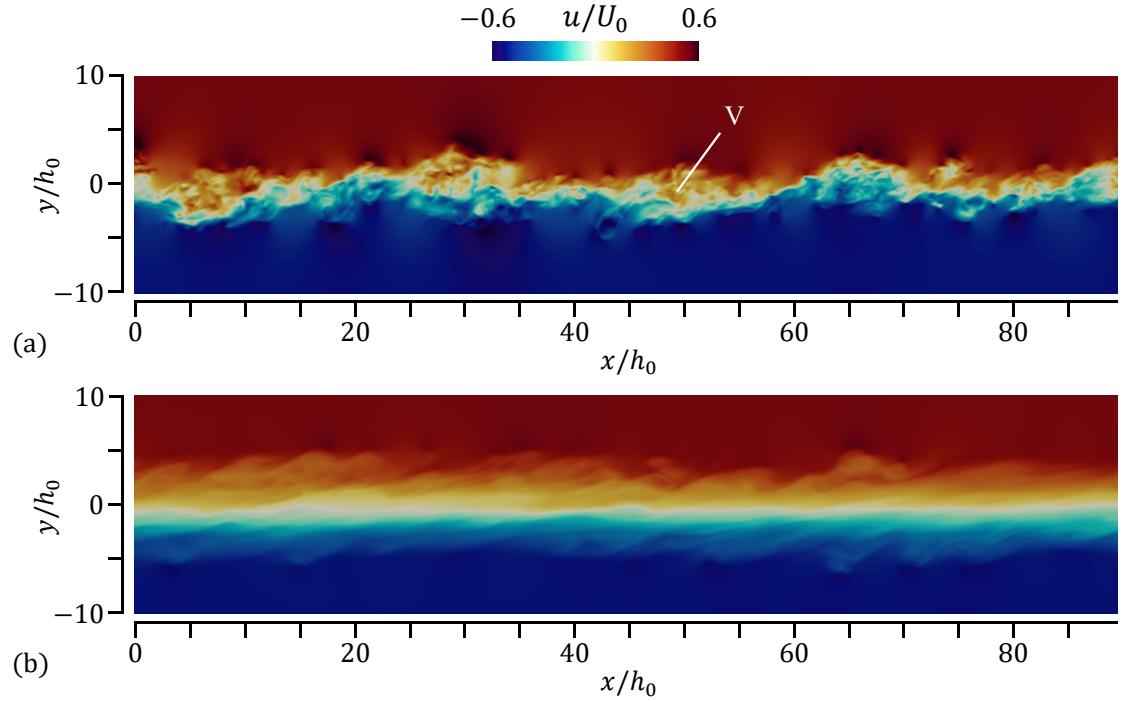

Fig. 3 The same as Fig. 2 but for $L_z = 84h_0$.

time. In each case, the simulation is advanced until $t = 320t_r$, where the reference time scale is defined as $t_r = h_0/U_0$. The number of grid points (N_x, N_y, N_z) is chosen such that the grid spacings remain smaller than twice the Kolmogorov length scale throughout the simulation. For the case with $L_z = 14h_0$, an additional DNS is performed with an increased number of grid points to examine grid dependence. The grid size is uniform in the x and z directions and non-uniform in the y direction. The y-direction grid is constructed using a hyperbolic tangent distribution, providing the finest

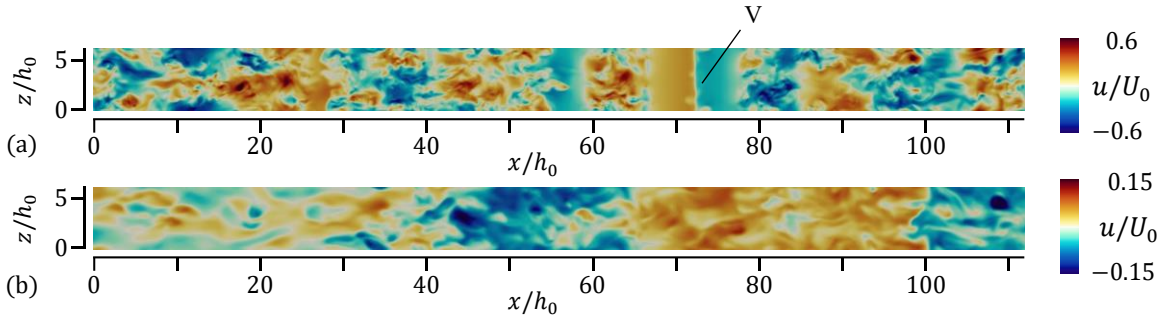

Fig. 4 Streamwise velocity profiles on the xz plane at the shear layer center ($y = 0$) at (a) $t/t_r = 120$ and (b) $t/t_r = 320$ for $L_z = 7h_0$.

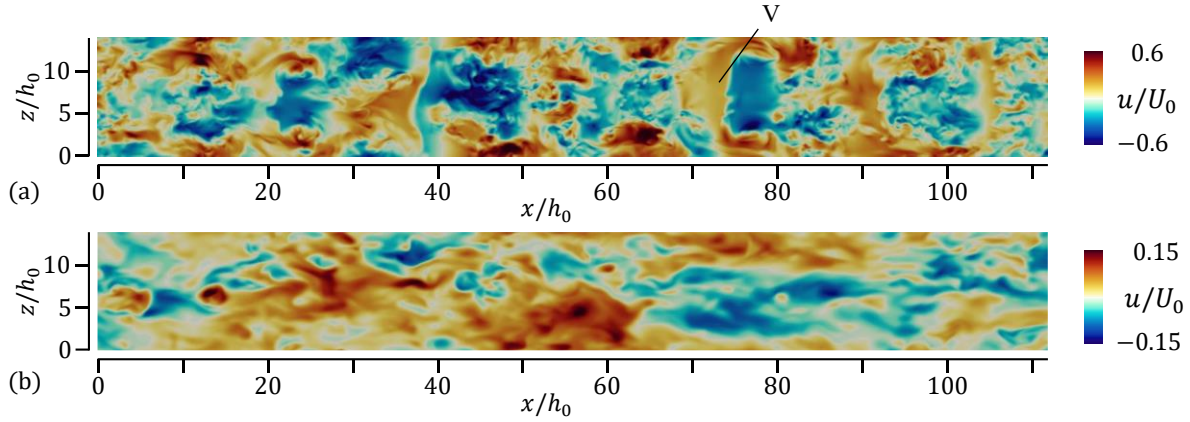

Fig. 5 The same as Fig. 4 but for $L_z = 14h_0$.

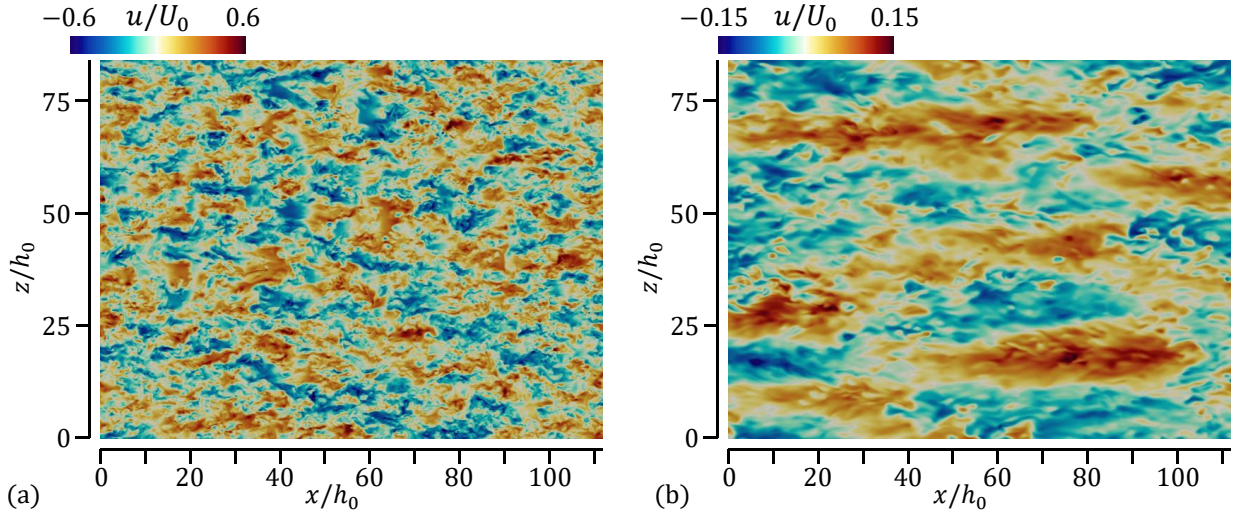

Fig. 6 The same as Fig. 4 but for $L_z = 84h_0$.

resolution at the center of the domain to accurately resolve the evolution of KH instability and the subsequent turbulent development, as discussed in previous studies (Watanabe et al., 2018a; Akao et al., 2022). The time increments are set to $0.0083t_r$ in case Lz14f and $0.01t_r$ in the other cases. Each simulation is repeated N_e times with different initial random velocity fluctuations. Statistical quantities are evaluated using ensemble averages over the N_e simulations in addition to spatial averaging on horizontal planes. The values of N_e for each case are also listed in Tab. 1. More simulations are performed for smaller domains since the statistical samples within a single simulation decrease as L_z

becomes smaller.

3. Results and discussion

3.1 Instantaneous flow fields

Figures 2 and 3 visualize instantaneous velocity profiles on an xy plane at $t = 120t_r$ and $320t_r$, for cases Lz07 and Lz84. The initial mean shear induces the KH instability, resulting in the formation of large-scale spanwise vortices, examples of which are marked as 'V' in each figure. These vortices subsequently collapse, leading to the development of fully three-dimensional turbulence, which decays over time. This transition process, as visualized on the xy plane, is similar for both cases. The detailed mechanisms of transition initiated by the KH instability have been documented in previous studies (Watanabe and Nagata, 2021; Fritts et al., 2024).

Figures 4, 5, and 6 show the streamwise velocity on horizontal planes at the center of the shear layer ($y = 0$) for cases Lz07, Lz14, and Lz84. The differences among the cases with different L_z values are clearly observed on the horizontal plane. At $t = 120t_r$, alternating bands of positive and negative velocity appear without small-scale fluctuations in cases Lz07 and Lz14, as marked by 'V'. These patterns are associated with spanwise vortices originating from KH instability. When L_z is small, these vortices persist for extended periods without breaking down into small-scale turbulence. In contrast, when the spanwise domain is sufficiently large, many KH vortices exhibit a meandering behavior, with their axes misaligned from the spanwise direction. This misalignment promotes interactions between neighboring vortices, accelerating their collapse and the onset of small-scale turbulence. As a result, Fig. 6(a) shows that small-scale velocity fluctuations are distributed across the entire horizontal plane, and the imprint of the initial KH vortices has disappeared. When L_z is small, confinement effects force each vortex to connect with itself via the periodic boundary. This suppressed misalignment inhibits vortex interaction, thereby delaying or preventing the generation of three-dimensional turbulence. This confinement effect during the transition is consistent with that reported for non-stratified shear layers (McMullan, 2015).

At $t = 320t_r$, the velocity distribution differs significantly from that at earlier times. In Fig. 6(b), for case Lz84, regions of positive and negative velocity are markedly elongated in the streamwise (x) direction. This anisotropic velocity pattern is associated with ELSS, whose streamwise length is much greater than those in the other directions. ELSS structures with positive and negative velocity appear alternately in the spanwise direction. A previous study demonstrated that the ELSS formation is driven by the mean shear effect enhanced by stable stratification (Akao et al., 2022). As L_z decreases, the spanwise arrangement of ELSS is altered because the distance between adjacent structures exceeds the spanwise domain size. In case Lz84, the streamwise length of ELSS reaches approximately $80h_0$, as estimated from the visible patterns of positive and negative velocity regions. Such elongated patterns are no longer observed in Lz07. In case Lz14, the spanwise organization of ELSS seen in Lz84 is not clearly captured, since the spanwise domain size is comparable to the width of a single ELSS structure.

In a stably stratified fluid, large-scale vertical motions are suppressed by buoyancy. Spanwise vortices, characterised by such vertical motions at their peripheries, are generated during the transition from the initial KH instability. Their presence is visible at $t = 120t_r$ in Figs. 2(a) and 5(a), but they weaken as the flow evolves due to buoyancy suppression (Smyth and Moum, 2000; Salehipour et al. 2015). When the spanwise domain size is large, interactions between neighbouring spanwise vortices rapidly lead to their breakdown at early times, although this interaction is inhibited by the finite-domain-size effect (Fritts et al., 2021; Watanabe and Nagata, 2021). For this reason, in Lz84 the spanwise vortices are already absent at $t = 120t_r$ in Figs. 2(b) and 5(b). Consequently, in the fully developed turbulent regime, large-scale spanwise vortices are not visible in the flow visualisations or in the correlation profile of Fig. 13.

For the same flow configuration examined here, vortex identification using the Q criterion was tested in our previous studies (Watanabe et al., 2016, 2019a). Vortices identified by the Q criterion are known to be nearly identical to those obtained with the λ_2 method (Kolář and Šístek, 2015). These schemes were found to be effective for visualizing small-scale vortices but do not reveal information on large-scale structures such as the ELSS. Large-scale features are more effectively examined using the velocity field, as velocity distributions are dominated by large-scale turbulent motions rather than by vortical motions. For this reason, velocity contours are used in the present study to characterize the spatial organization of ELSS. It should be noted that turbulent structures are not necessarily equivalent to vortices, and the ELSS discussed here are not characterized by strong vortical motions.

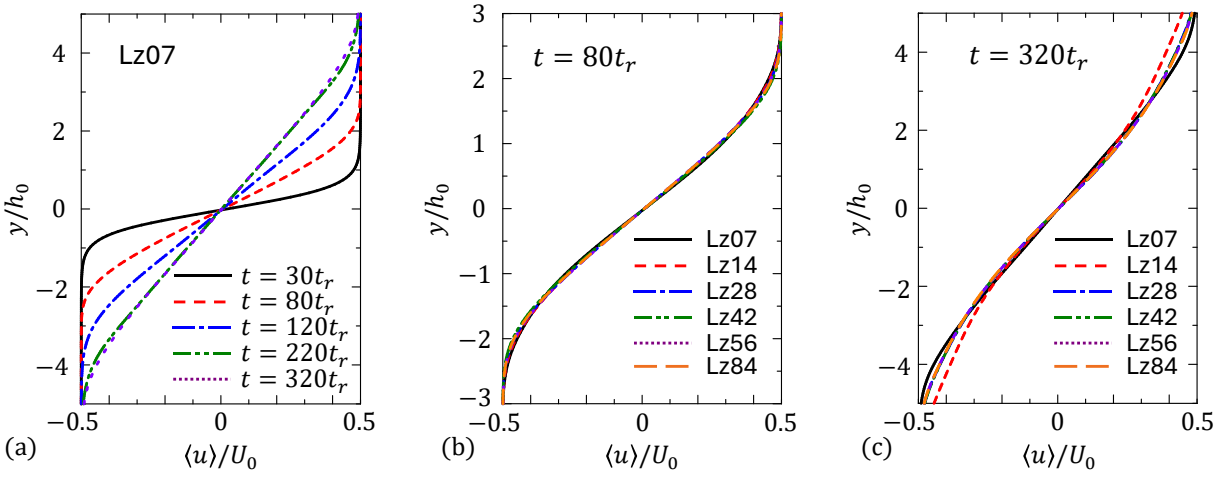

Fig. 7 Vertical profiles of mean streamwise velocity $\langle u \rangle$: (a) temporal evolution in Lz04; (b), (c) L_z dependence at (b) $t/t_r = 80$ and (c) $t/t_r = 320$.

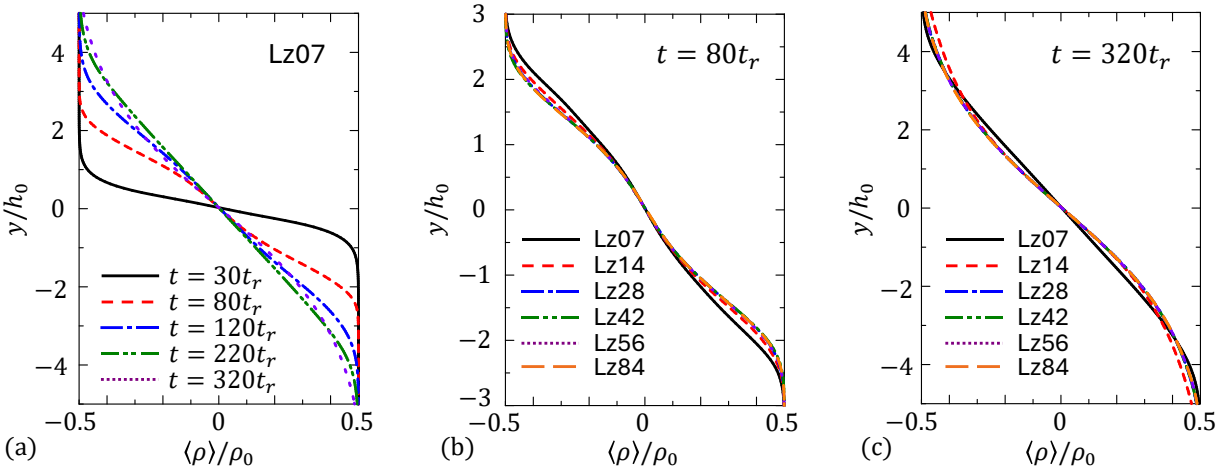

Fig. 8 Vertical profiles of mean density $\langle \rho \rangle$: (a) temporal evolution in Lz04; (b), (c) L_z dependence at (b) $t/t_r = 80$ and (c) $t/t_r = 320$.

3.2 One-point statistics of velocity and density

Flow visualizations have confirmed that spanwise confinement at small L_z alters the transition process and ELSS formation. The onset of these effects on the statistical behavior is examined below, beginning with one-point statistics of velocity and density, followed by spectral and spatial correlation analyses in the next subsection.

Figure 7(a) shows the temporal variation of the vertical distribution of the mean streamwise velocity $\langle u \rangle$ in case Lz07. Initially, the mean velocity varies within a thin shear layer of thickness h_0. As the turbulent shear layer develops, vertical momentum transport causes the mean velocity distribution to broaden. Since turbulent transport is more active at earlier times, the mean velocity shows minimal variation at later times as turbulence decays. This evolution of the mean velocity profile is consistent with previous studies on stably stratified shear layers (Smyth and Moum, 2000; Watanabe et al., 2016). Figures 7(b) and (c) compare the mean velocity profiles at $t = 80t_r$ and $320t_r$ for different L_z cases. At early times, the mean velocity profile is largely insensitive to L_z. However, at later times, the profiles in cases Lz07 and Lz14 exhibit noticeable deviations from those in cases with larger L_z, although the differences are relatively small and remain within the magnitude of the corresponding turbulent fluctuations discussed below.

Figure 8 provides similar comparisons for the mean density profiles. Figure 8(a) shows the temporal variation in case Lz07. Initially, the shear layer exhibits a distinct density jump at $y = 0$. As the turbulent shear layer develops, the mean density profile broadens. Similar to the mean velocity, the mean density profile shows little temporal variation at later

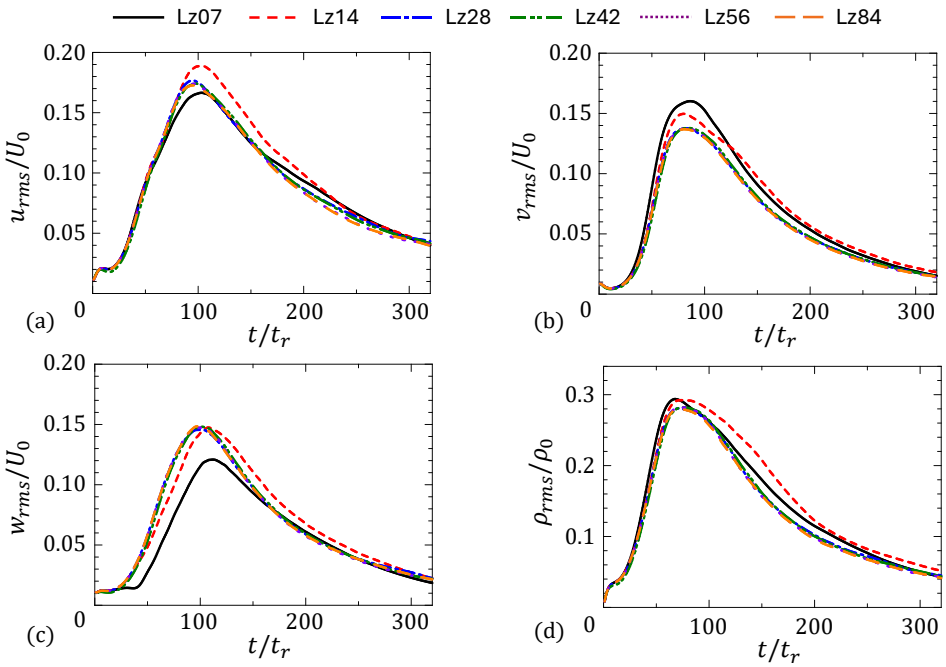

Fig. 9 Temporal variations of rms fluctuations of velocity and density at the shear layer center ($y = 0$): (a) u_{rms}, (b) v_{rms}, (c) w_{rms}, and (d) ρ_{rms}.

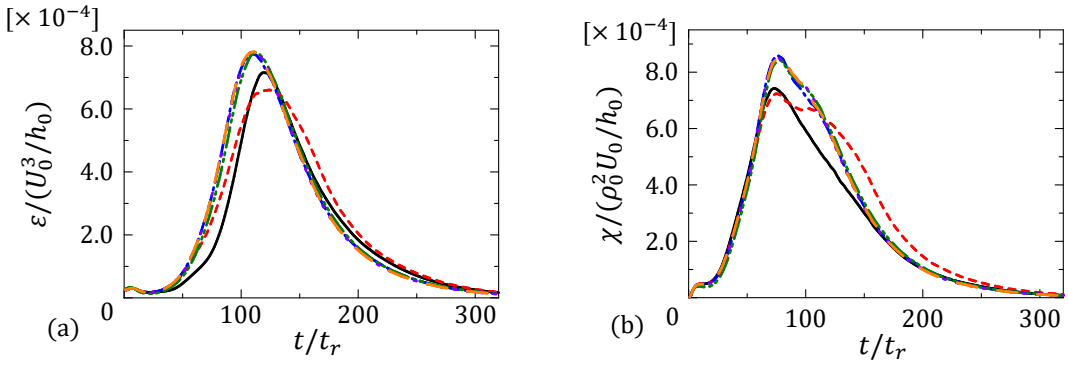

Fig. 10 Temporal variations of the dissipation rates in turbulent kinetic energy and density variance at the shear layer center ($y = 0$).

times due to the decay of turbulence. Figures 8(b) and (c) indicate that the mean density profiles in cases Lz07 and Lz14 deviate from those observed in cases with larger L_z.

Figure 9 compares the temporal variations of root-mean-squared (rms) velocity and density fluctuations. Until $t \approx 100t_r$, the fluctuations increase due to turbulence generation by KH instability, and subsequently decrease as turbulence decays. As observed in the mean velocity and density profiles, cases Lz07 and Lz14 exhibit different fluctuation behaviors compared to larger L_z cases. Specifically, the spanwise rms velocity fluctuation w_{rms} is notably smaller in Lz07 during the transition phase ($t < 100t_r$). This is attributed to the sustained KH vortices discussed earlier, which are quasi-two-dimensional and lack significant spanwise velocity fluctuations. In contrast, larger L_z values allow for the rapid breakdown of vortices, leading to the development of three-dimensional turbulence with larger w_{rms}. Correspondingly, the vertical rms velocity fluctuation v_{rms} is larger in Lz07 during the transition phase, as the KH vortices with strong vertical velocity components persist for a longer time. While Lz14 also shows deviations from larger L_z cases, the differences are less pronounced in the transitional regime ($t < 100t_r$), and the transition process is not entirely altered by spanwise confinement. Instead, the differences become more evident in the decay regime following the transition ($t > 100t_r$).

Figure 10 compares the dissipation rates of turbulent kinetic energy and density variance, defined respectively as $\varepsilon = \nu\langle(\partial u_i'/\partial x_j)^2\rangle$ and $\chi = \kappa\langle(\partial\rho'/\partial x_j)^2\rangle$. Both Lz07 and Lz14 exhibit notable differences from the larger L_z cases.

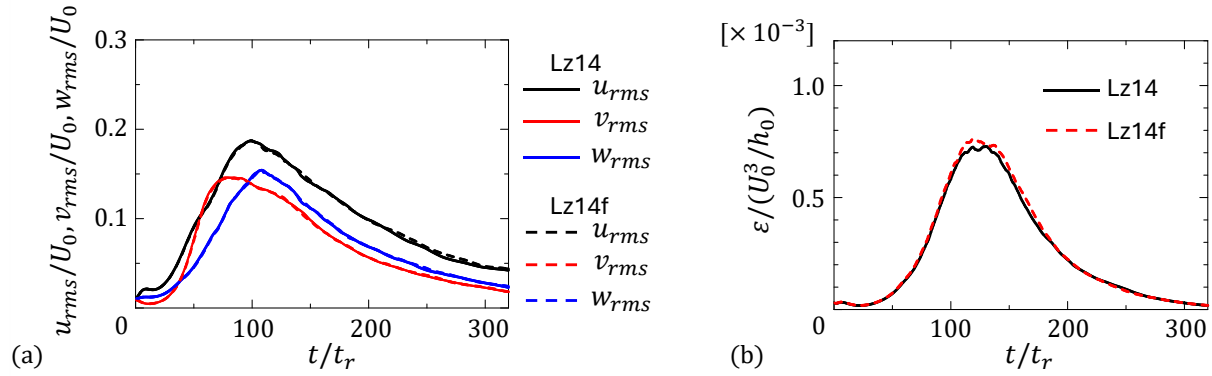

Fig. 11 Comparisons of (a) rms velocity fluctuations and (b) the turbulent kinetic energy dissipation rate between Lz14 and Lz14f.

These dissipation rates are determined by the velocity and density gradients, which are governed by small-scale turbulent motions. The delayed formation of three-dimensional small-scale turbulence in cases with small L_z leads to reduced dissipation rates during the transition phase.

The comparisons of one-point statistics reveal that spanwise confinement affects flow evolution for $L_z \leq 14h_0$. More specifically, $L_z = 7h_0$ is insufficient to resolve the initial transition process, and the rms fluctuations in the spanwise and vertical velocities are significantly altered by confinement effects. For $L_z = 14h_0$, the transition process remains similar to that in large L_z cases; however, the late-time behavior after the transition is still influenced by the limited domain size.

Figure 11 compares the rms velocity fluctuations and the turbulent kinetic energy dissipation rate between cases Lz14 and Lz14f. The results are presented for a single DNS run without ensemble averaging, and both cases utilise the same random number set to generate initial velocity fluctuations. These two cases employ computational grids with different spatial resolutions. The results indicate that resolution has little influence on the temporal variations of these quantities. This is because the grid size in Lz14 is already sufficient to resolve the small-scale velocity and density fluctuations, as confirmed by the grid-dependence tests of the present numerical schemes (Watanabe et al., 2018a).

3.3 Energy spectra and auto-correlation functions

The relevance of spanwise domain size to flow behavior is further explored through analyses of energy spectra and auto-correlation functions. This study focuses on confinement effects after the transition, which are likely related to the formation of ELSS. The spectra and correlations are evaluated for the streamwise velocity, as its spatial distribution characterizes the organization of ELSS.

We denote the Fourier transform of u in the streamwise direction as $\hat{u}(k_x, y, z, t)$, and its complex conjugate as $\hat{u}^*$, where k_x is the streamwise wavenumber. The energy spectrum of u is defined as $E_u(k_x, y, t) = \mathrm{R}(\langle \hat{u}\hat{u}^* \rangle)$, where $\mathrm{R}(f)$ denotes the real part of the complex variable f. The average $\langle \hat{u}\hat{u}^* \rangle$ is computed using spanwise averaging and ensemble averages over repeated simulations.

This study considers the correlation of u between two points separated on a horizontal plane. The two-point correlation function is defined as

$$C_{uxz} = \frac{\langle u'(x, y, z, t) u'(x + r_x, y, z + r_z, t) \rangle}{u_{rms}^2(y, t)}. \tag{4}$$

Previous studies have shown that ELSS structures develop near the center of the shear layer and do not extend into the intermittent region (Watanabe et al., 2019a), where turbulent and non-turbulent fluids coexist and are separated by an interface (Watanabe et al., 2017a; Neamtu-Halic et al., 2019). Therefore, the energy spectrum and correlation function are evaluated at the center of the shear layer.

Figure 12 presents the energy spectra at different time instances for all simulation cases. The spectra are plotted against the streamwise wavelength $\lambda_x = 2\pi/k_x$, and are premultiplied by k_x. When shown on a logarithmic scale, the premultiplied spectrum is useful because the area under the curve visually represents the energy contribution from a

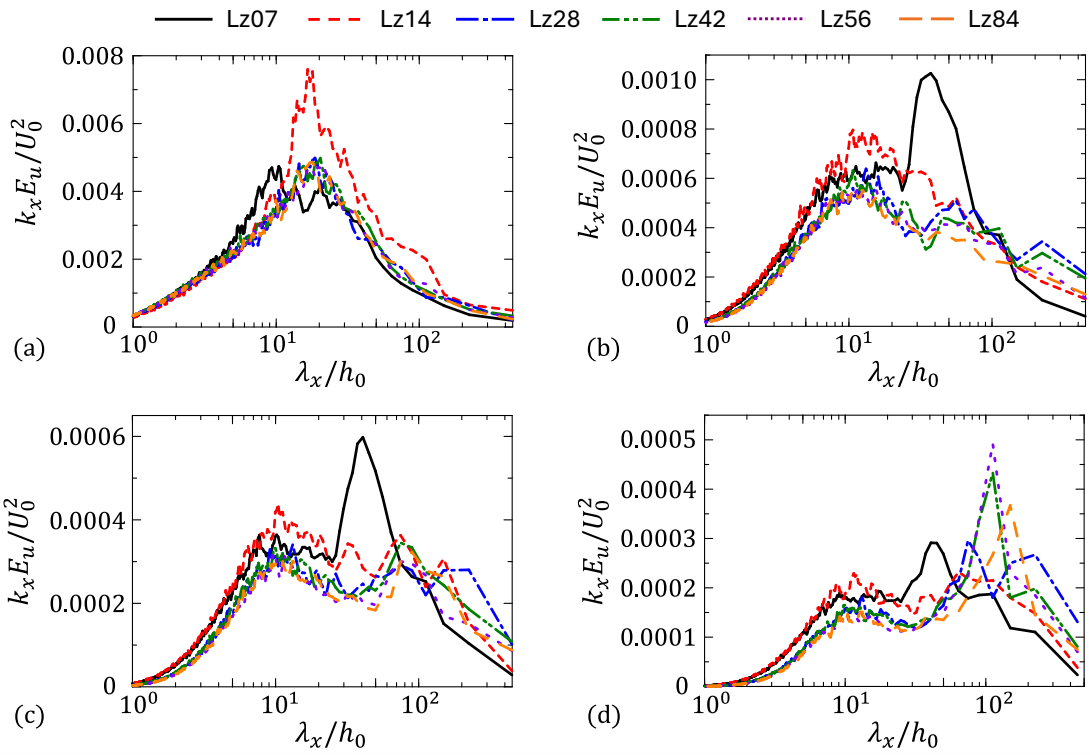

Fig. 12 Streamwise-wavenumber spectra of streamwise velocity $E_u(k_x)$ at $y = 0$ at (a) $t = 120t_r$, (b) $t = 240t_r$, (c) $t = 280t_r$, and (d) $t = 320t_r$. The spectra, premultiplied by streamwise wavenumber k_x, are plotted against wavelength ($\lambda_x = 2\pi/k_x$).

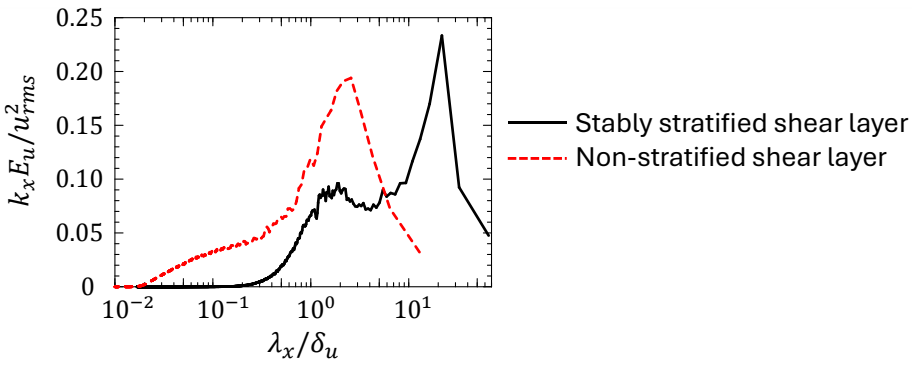

Fig. 13 Comparisons of the premultipled spectra $k_x E_u$ normalized by rms velocity fluctuations, u_{rms}, between stably-stratified shear layer (Lz84) and non-stratified shear layer with $Ri = 0$ (Watanabe and Nagata, 2021). The spectra evaluated at $y = 0$ and $t = 320t_r$ are plotted against wavelength ($\lambda_x = 2\pi/k_x$) normalized by the shear layer thickness δ_u.

specific wavelength range in the logarithmic axis. This is evident when the relation $u_{rms}^2 = \int_0^\infty E_u dk_x$ is rewritten as

$$u_{rms}^2 = \int_0^\infty k_x E_u d(\log k_x) = (\log 2\pi) \int_0^\infty k_x E_u d(\log \lambda_x). \tag{5}$$

The temporal evolution of the spectrum in Lz84 is consistent with previous studies of ELSS (Watanabe and Nagata, 2021). At $t = 120t_r$ in Fig. 12(a), the spectrum exhibits a single peak at $\lambda_x/h_0 \approx 20$. By $t = 240t_r$ in Fig. 12(b), this peak shifts to a smaller wavelength, $\lambda_x/h_0 \approx 10$. Subsequently, a secondary peak emerges at a much larger scale,

around $\lambda_x/h_0 \approx 10^2$, which begins to dominate at $t = 280t_r$ in Fig. 12(c), and surpasses the smaller-wavelength peak by $t = 320t_r$ in Fig. 12(d). This large-wavelength peak is associated with ELSS formation, as visually observed in the streamwise velocity distributions in Fig. 6(b). By $t = 320t_r$, the formation of the large-scale peak at $\lambda_x/h_0 \approx 10^2$ is complete in cases Lz42, Lz56, and Lz84. In smaller L_z cases, however, this secondary peak remains weak even at $t = 320t_r$. Notably, the spectral shape in Lz07 and Lz14 differs significantly from early times. Despite all simulations using the same streamwise domain size $L_x = 448h_0$, differences in L_z lead to substantial variations in the streamwise velocity distribution.

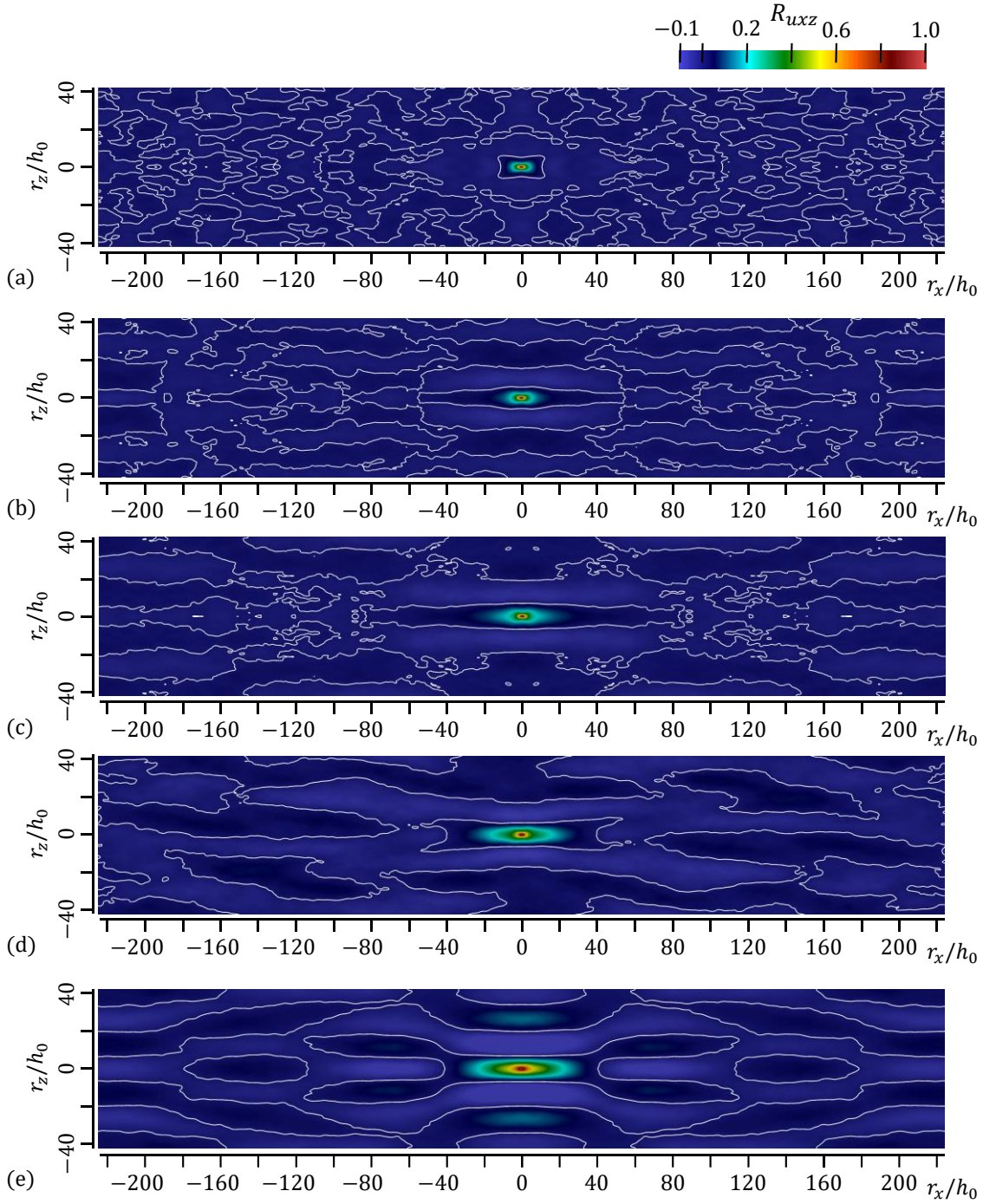

Fig. 14 Two-dimensional auto-correlation functions of streamwise velocity, $R_{uxz}(r_x, r_z, y, t)$, at $y = 0$ in Lz84: (a) $t = 160t_r$; (b) $t = 200t_r$; (c) $t = 240t_r$; (d) $t = 280t_r$; (e) $t = 320t_r$. The white lines indicate the isovalue contours of $R_{uxz} = 0$.

Figure 13 compares the streamwise energy spectra for the present stably stratified case and a non-stratified case ($Ri = 0$) from Watanabe and Nagata (2021). The spectra are plotted against the streamwise wavelength normalized by the shear layer thickness δ_u, which is defined as the distance between two locations of $\langle u \rangle / U_0 = \pm 0.49$. In the non-stratified case, the spectrum exhibits a single peak at a wavelength comparable to the shear layer thickness, corresponding to the characteristic large-scale structures whose size scales with the layer thickness. In contrast, the stably stratified case shows two distinct peaks: the shorter peak wavelength is again close to the shear layer thickness, while the longer wavelength—about times larger—is associated with the ELSS described in this study. The absence of the spectral peak at $\lambda_x / \delta_u \approx 20$ in the constant-density case indicates that ELSS do not form without stable stratification. This behaviour is consistent with the understanding that ELSS formation occurs when the vertical growth of the turbulent shear layer is inhibited by buoyancy effects (Akao et al., 2022).

Figure 14 presents the temporal variations of the two-point correlation function $R_{uxz}(r_x, r_z)$ at $y = 0$ for case Lz84. By definition, the correlation satisfies $R_{uxz}(r_x, r_z) = 1$ at $(r_x, r_z) = (0, 0)$ and decreases as r_x and r_z increase. The correlation distribution on the (r_x, r_z) plane reflects the shape and configuration of turbulent structures. At early times, large correlation values are concentrated near the origin. As time progresses, the correlation pattern extends in the r_x direction, corresponding to the formation of ELSS, which contributes to long-range correlations in the streamwise direction. At $t = 160 t_r$, the isoline of $R_{uxz} = 0$ reflects statistical oscillations around zero at large r_x and r_z, exhibiting no coherent pattern. At later times, the isoline becomes more distinct, indicating the establishment of large-

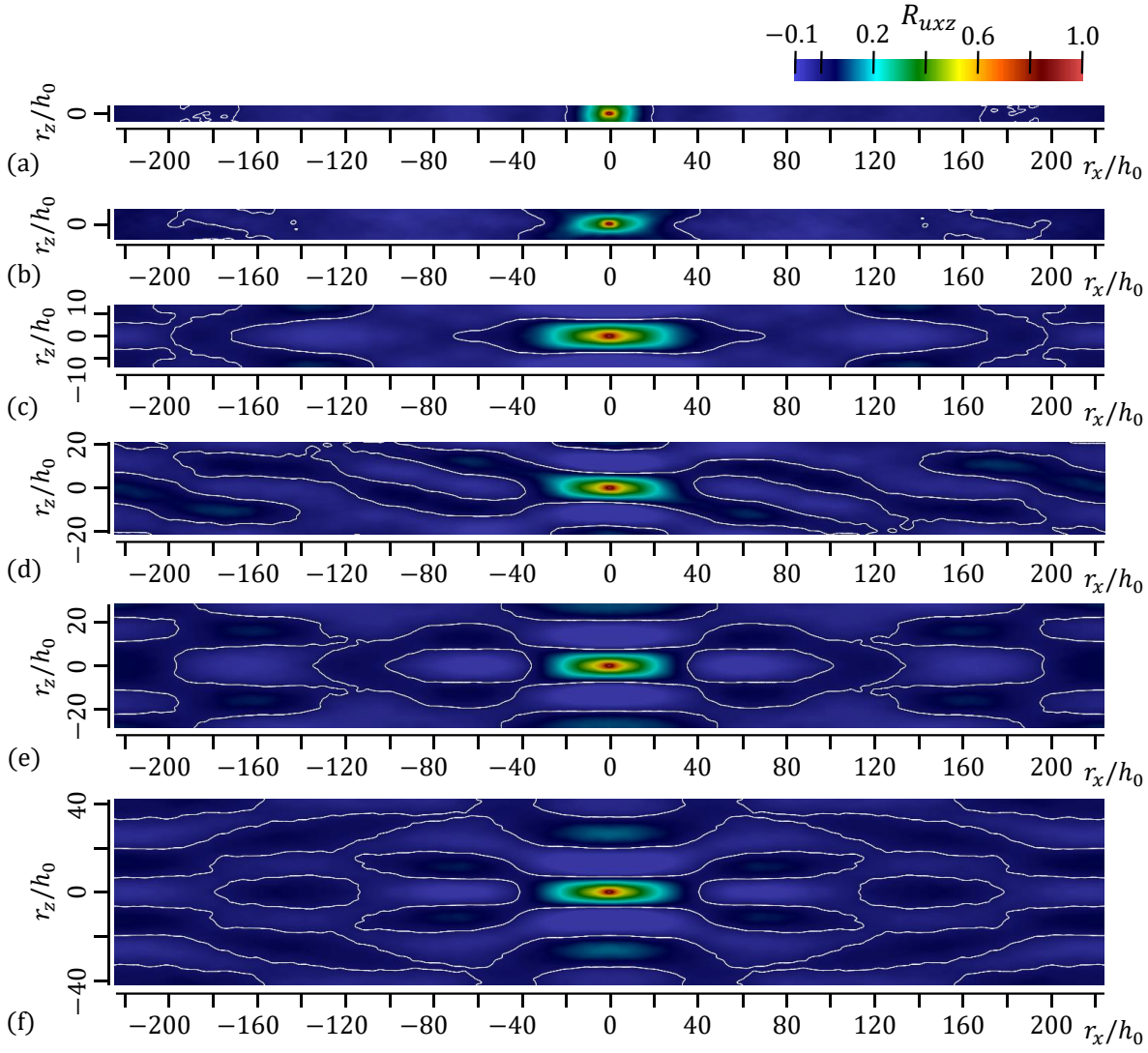

Fig. 15 Two-dimensional auto-correlation functions of streamwise velocity, $R_{uxz}(r_x, r_z, y, t)$, at $y = 0$ and $t = 320 t_r$, for (a) Lz07, (b) Lz14, (c) Lz28, (d) Lz42, (e) Lz56, and (f) Lz84.

scale correlations due to ELSS formation. The ELSS organize the correlation structure over large r_x and r_z distances. At $t = 320t_r$, the positive correlation near the origin exhibits an "X" pattern, reflecting the meandering nature of ELSS, which are not perfectly aligned with the streamwise direction. A similar correlation pattern was also reported in wall turbulence, where turbulent structures similar to ELSS also develop near the wall (Hutchins and Marusic, 2007). This meandering leads to the slanted correlation structure. Along the r_z axis at $r_x = 0$, the correlation function oscillates around zero: R_{uxz} decreases to zero at $r_z \approx 8h_0$, reaches a minimum at $r_z \approx 12h_0$, and attains a local maximum at $r_z \approx 25h_0$. This oscillation arises from multiple ELSS with alternating signs of streamwise velocity appearing in the spanwise direction. The visualization in Fig. 6(b) confirms this configuration, showing elongated regions of $u > 0$ and $u < 0$ alternating along the z axis. This characteristic ELSS structure is well captured in the correlation profile. The correlation profiles show no evidence of spanwise vortical structures, indicating that such structures formed during the initial transition phase do not influence the subsequent ELSS evolution.

Figure 15 compares the two-point correlation function at $y = 0$ and $t = 320t_r$ for different L_z cases. The characteristic "X" pattern observed in the correlation function disappears when $L_z \leq 28h_0$. In case Lz28, negative R_{uxz} values are observed at $r_z = 10h_0$ and $r_x = 0$, indicating that ELSS with opposite signs of streamwise velocity alternatively appear in the spanwise direction. The large positive correlation is distributed around $(r_x, r_z) = (0, 0)$ over a similar range of r_x as in larger L_z cases, suggesting that ELSS with long streamwise extent still form. However, in Lz28, the positive correlation extends only along the r_x axis at $r_z = 0$, lacking the "X" pattern. This implies that the meandering feature of ELSS is no longer present. Further reduction in L_z, as in cases Lz07 and Lz14, causes the region of large positive correlation to become confined to small $|r_x|$. Thus, ELSS fail to develop when $L_z \leq 14h_0$, even though the streamwise extent of the computational domain is much larger than the typical ELSS size.

The spanwise domain size significantly influences the one-point velocity and density statistics when L_z is smaller than $14h_0$, as shown in Sec. 3.2. While the Lz28 case fails to capture the meandering feature of ELSS, the spanwise distribution of multiple ELSS is similar to that in larger L_z cases, as evidenced by the two-point correlation function. Nevertheless, Lz28 produces variations in one-point statistics that are comparable to those in larger L_z cases. This suggests that, although the meandering feature is a prominent characteristic of ELSS, it is not the dominant factor governing flow statistics. Instead, the presence of multiple ELSS with alternating positive and negative streamwise velocity fluctuations in the spanwise direction plays a more critical role. This interpretation is further supported by the differences between Lz14 and larger L_z cases, as the Lz14 case fails to reproduce multiple rows of ELSS in the spanwise direction.

4. Conclusion

This study investigated the effects of spanwise domain size on the development and statistical properties of stably stratified turbulent shear layers using direct numerical simulations. Special attention was given to the formation and organization of elongated large-scale structures (ELSS), which are known to dominate the streamwise velocity field in such flows. Flow visualizations, one-point statistics, energy spectra, and two-point correlation functions demonstrated that the spanwise confinement significantly alters the transition process and ELSS formation when $L_z \leq 14h_0$. In particular, the case with $L_z = 7h_0$ failed to capture the transition to fully developed turbulence, and exhibited suppressed spanwise velocity fluctuations during the transition. The $L_z = 14h_0$ case reproduced the transition process but deviated from larger L_z cases in the decay regime. The analysis of energy spectra revealed that the emergence of a secondary spectral peak at long wavelengths, associated with ELSS formation, requires a sufficiently large spanwise domain. Correlation analyses confirmed that meandering ELSS contribute to long-range spatial organization in the streamwise and spanwise directions. However, simulations with limited L_z, such as Lz28, indicated that the meandering of ELSS is not essential to capturing the bulk flow statistics, provided that multiple ELSS can still be represented across the span. While the meandering feature of ELSS influences the flow structure, the presence of multiple alternating ELSS in the spanwise direction plays a more decisive role in determining the statistical behavior of the flow.

Acknowledgments and conflicts of interest

Numerical simulations were performed by the high-performance computing systems at the Japan Agency for Marine-Earth Science and Technology. This work was supported by JSPS KAKENHI Grant Nos. 23K22669 and 25K01155.

There are no any conflict of interest regarding the content of the manuscript. The authors have no conflicts to disclose.

References

Akao, T., Watanabe, T. and Nagata, K., Vertical confinement effects on a fully developed turbulent shear layer, Physics of Fluids, Vol. 34, 055129 (2022), DOI:10.1063/5.0090686.

Cimbala, J. M., Nagib, H. M. and Roshko, A., Large structure in the far wakes of two-dimensional bluff bodies, Journal of Fluid Mechanics, Vol. 190, pp. 265–298 (1988).

Fritts, D. C., Wieland, S. A., Lund, T. S. and Thorpe, S. A., Kelvin--Helmholtz billow interactions and instabilities in the mesosphere over the Andes Lidar Observatory: 2. Modeling and interpretation, Journal of Geophysical Research: Atmospheres, Vol. 126, e2020JD033412 (2021), DOI:10.1002/2014JD021833.

Fritts, D. C., Wang, L., Lund, T. S. and Thorpe, S. A., Multi-scale dynamics of Kelvin–Helmholtz instabilities. Part 1. Secondary instabilities and the dynamics of tubes and knots, Journal of Fluid Mechanics, Vol. 941, A30 (2022), DOI:10.1017/jfm.2021.1085.

Fritts, D. C., Wang, L., Lund, T. and Geller, M. A., Kelvin–Helmholtz Instability "Tube" and "Knot" Dynamics. Part III: Extension of Elevated Turbulence and Energy Dissipation into Increasingly Viscous Flows, Journal of the Atmospheric Sciences, Vol. 81, pp. 1147–1164 (2024).

Gualtieri, P. and Meneveau, C., Direct numerical simulations of turbulence subjected to a straining and destraining cycle, Physics of Fluids, Vol. 22, 065104 (2010), DOI:10.1063/1.3453709.

Hayashi, M., Watanabe, T. and Nagata, K., Characteristics of small-scale shear layers in a temporally evolving turbulent planar jet, Journal of Fluid Mechanics, Vol. 920, A38 (2021a), DOI:10.1017/jfm.2021.459.

Hayashi, M., Watanabe, T. and Nagata, K., The relation between shearing motions and the turbulent/non-turbulent interface in a turbulent planar jet, Physics of Fluids, Vol. 33, 055126 (2021b), DOI:10.1063/5.0045376.

Hutchins, N. and Marusic, I., Evidence of very long meandering features in the logarithmic region of turbulent boundary layers, Journal of Fluid Mechanics, Vol. 579, pp. 1–28 (2007).

Jiménez, J. and Moin, P., The minimal flow unit in near-wall turbulence, Journal of Fluid Mechanics, Vol. 225, pp. 213–240 (1991).

Kolář, K. and Šístek, J., Corotational and compressibility aspects leading to a modification of the vortex-identification Q-criterion, AIAA Journal, Vol. 53, pp. 2406–2410 (2015).

Mashayek, A. and Peltier, W. R., The 'zoo' of secondary instabilities precursory to stratified shear flow transition. Part 1: Shear aligned convection, pairing, and braid instabilities, Journal of Fluid Mechanics, Vol. 708, pp. 5–44 (2012a).

Mashayek, A. and Peltier, W. R., The 'zoo' of secondary instabilities precursory to stratified shear flow transition. Part 2: The influence of stratification, Journal of Fluid Mechanics, Vol. 708, pp. 45–70 (2012b).

McMullan, W. A., Spanwise domain effects on the evolution of the plane turbulent mixing layer, International Journal of Computational Fluid Dynamics, Vol. 29, pp. 333–345 (2015).

McMullan, W. A., Mifsud, J. and Angelino, M., The growth of the initially turbulent mixing layer: A large eddy simulation study, Physics of Fluids, Vol. 36, 115194 (2024), DOI:10.1063/5.0238956.

Nakamura, K., Watanabe, T. and Nagata, K., Turbulent/turbulent interfacial layers of a shearless turbulence mixing layer in temporally evolving grid turbulence, Physics of Fluids, Vol. 35, 045117 (2023), DOI:10.1063/5.0141253.

Neamtu-Halic, M. M., Krug, D., Haller, G. and Holzner, M., Lagrangian coherent structures and entrainment near the turbulent/non-turbulent interface of a gravity current, Journal of Fluid Mechanics, Vol. 877, pp. 824–843 (2019).

Okino, S., Akiyama, S., Takagi, K. and Hanazaki, H., Density distribution in the flow past a sphere descending in a salt-stratified fluid, Journal of Fluid Mechanics, Vol. 927, A15 (2021), DOI:10.1017/jfm.2021.758.

Onishi, R. and Komori, S., Thermally stratified liquid turbulence with a chemical reaction, AIChE Journal, Vol. 52, pp. 456–468 (2006).

Rahmani, M., Lawrence, G. A. and Seymour, B. R., The effect of Reynolds number on mixing in Kelvin–Helmholtz billows, Journal of Fluid Mechanics, Vol. 759, pp. 612–641 (2014).

Salehipour, H., Peltier, W. R. and Mashayek, A., Turbulent diapycnal mixing in stratified shear flows: the influence of Prandtl number on mixing efficiency and transition at high Reynolds number, Journal of Fluid Mechanics, Vol. 773, pp. 178–223 (2015).

Salehipour, H., Caulfield, C. C. and Peltier, W. R., Turbulent mixing due to the Holmboe wave instability at high Reynolds

number, Journal of Fluid Mechanics, Vol. 803, pp. 591–621 (2016).
Smyth, W. D. and Moum, J. N., Length scales of turbulence in stably stratified mixing layers, Physics of Fluids, Vol. 12, pp. 1327–1342 (2000).
Smyth, W. D. and Moum, J. N., Ocean mixing by Kelvin–Helmholtz instability, Oceanography, Vol. 25, pp. 140–149 (2012).
Smyth, W. D. and Winters, K. B., Turbulence and mixing in Holmboe waves, Journal of Physical Oceanography, Vol. 33, pp. 694–711 (2003).
Smyth, W. D., Carpenter, J. R. and Lawrence, G. A., Mixing in symmetric Holmboe waves, Journal of Physical Oceanography, Vol. 37, pp. 1566–1583 (2007).
Watanabe, T., Riley, J. J. and Nagata, K., Effects of stable stratification on turbulent/nonturbulent interfaces in turbulent mixing layers, Physical Review Fluids, Vol. 1, 044301 (2016), DOI:10.1103/PhysRevFluids.1.044301.
Watanabe, T., Riley, J. J. and Nagata, K., Turbulent entrainment across turbulent–nonturbulent interfaces in stably stratified mixing layers, Physical Review Fluids, Vol. 2, 104803 (2017a), DOI:10.1103/PhysRevFluids.2.104803.
Watanabe, T. and Nagata, K., Gradients estimation from random points with volumetric tensor in turbulence, Journal of Computational Physics, Vol. 350, pp. 518–529 (2017b).
Watanabe, T., Riley, J. J., Nagata, K., Onishi, R. and Matsuda, K., A localized turbulent mixing layer in a uniformly stratified environment, Journal of Fluid Mechanics, Vol. 849, pp. 245–276 (2018a).
Watanabe, T. and Nagata, K., Integral invariants and decay of temporally developing grid turbulence, Physics of Fluids, Vol. 30, 105111 (2018b), DOI:10.1063/1.5045589.
Watanabe, T., Zhang, X. and Nagata, K., Turbulent/non-turbulent interfaces detected in DNS of incompressible turbulent boundary layers, Physics of Fluids, Vol. 30, 035102 (2018c), DOI:10.1063/1.5022423.
Watanabe, T., Riley, J. J., Nagata, K., Matsuda, K. and Onishi, R., Hairpin vortices and highly elongated flow structures in a stably stratified shear layer, Journal of Fluid Mechanics, Vol. 878, pp. 37–61 (2019a).
Watanabe, T., Zhang, X. and Nagata, K., Direct numerical simulation of incompressible turbulent boundary layers and planar jets at high Reynolds numbers initialized with implicit large eddy simulation, Computers & Fluids, Vol. 194, 104314 (2019b), DOI:10.1016/j.compfluid.2019.104314.
Watanabe, T. and Nagata, K., Large-scale characteristics of a stably stratified turbulent shear layer, Journal of Fluid Mechanics, Vol. 927, A27 (2021), DOI:10.1017/jfm.2021.773.
Watanabe, T., Zheng, Y. and Nagata, K., The decay of stably stratified grid turbulence in a viscosity-affected stratified flow regime, Journal of Fluid Mechanics, Vol. 946, A29 (2022), DOI:10.1017/jfm.2022.617.
Watanabe, T., Efficient enhancement of turbulent entrainment by small-scale shear instability, Journal of Fluid Mechanics, Vol. 988, A20 (2024), DOI:10.1017/jfm.2024.427.
Watanabe, T. and Nagata, K., Influences of small-scale shear instability on passive-scalar mixing in a shear-free turbulent front, Journal of Fluid Mechanics, Vol. 1008, A20 (2025), DOI:10.1017/jfm.2025.88.
Zhai, X. M. and Yeung, P. K., Evolution of anisotropy in direct numerical simulations of MHD turbulence in a strong magnetic field on elongated periodic domains, Physical Review Fluids, Vol. 3, 084602 (2018), DOI:10.1103/PhysRevFluids.3.084602.
Zhang, X., Watanabe, T. and Nagata, K., Reynolds number dependence of the turbulent/non-turbulent interface in temporally developing turbulent boundary layers, Journal of Fluid Mechanics, Vol. 964, A8 (2023), DOI: 10.1017/jfm.2023.329.